Faraday Discussions

Cite this: *Faraday Discuss.*, 2023, **245**, 352

PAPER

View Article Online
View Journal | View Issue

Open Access Article. Published on 06 2023. Downloaded on 01.02.26 6:57:40.
This article is licensed under a Creative Commons Attribution 3.0 Unported Licence.

Experimental radiative cooling rates of a polycyclic aromatic hydrocarbon cation

José E. Navarro Navarrete,[a] James N. Bull,[b] Henrik Cederquist,[a] Suvasthika Indrajith,[a] MingChao Ji,[a] Henning T. Schmidt,[a] Henning Zettergren,[a] Boxing Zhu[a] and Mark H. Stockett *[a]

Received 10th January 2023, Accepted 6th February 2023
DOI: 10.1039/d3fd00005b

Several small Polycyclic Aromatic Hydrocarbons (PAHs) have been identified recently in the Taurus Molecular Cloud (TMC-1) using radio telescope observations. Reproducing the observed abundances of these molecules has been a challenge for astrochemical models. Rapid radiative cooling of PAHs by Recurrent Fluorescence (RF), the emission of optical photons from thermally populated electronically excited states, has been shown to efficiently stabilize small PAHs following ionization, augmenting their resilience in astronomical environments and helping to rationalize their observed high abundances. Here, we use a novel method to experimentally determine the radiative cooling rate of the cation of 1-cyanonaphthalene ($C_{10}H_7CN$, 1-CNN), the neutral species of which has been identified in TMC-1. Laser-induced dissociation rates and kinetic energy release distributions of 1-CNN cations isolated in a cryogenic electrostatic ion-beam storage ring are analysed to track the time evolution of the vibrational energy distribution of the initially hot ion ensemble as it cools. The measured cooling rate is in good agreement with the previously calculated RF rate coefficient. Improved measurements and models of the RF mechanism are needed to interpret astronomical observations and refine predictions of the stabilities of interstellar PAHs.

1 Introduction

In 2021, after decades of inconclusive searches, astronomers identified the first specific Polycyclic Aromatic Hydrocarbon (PAH) molecules in space.[1] Using the Greenbank Radio Telescope, McGuire *et al.* identified two isomers of the small PAH cyanonaphthalene (CNN, $C_{10}H_7CN$) in the Taurus Molecular Cloud (TMC-1). Several other aromatics have been identified using similar methods[2] and many more likely await discovery. Meanwhile, JWST promises to provide new insight into the properties and evolution of interstellar PAHs through observations of their infrared emission bands.[3,4]

[a]*Department of Physics, Stockholm University, Stockholm, Sweden. E-mail: Mark.Stockett@fysik.su.se*
[b]*School of Chemistry, University of East Anglia, Norwich, UK*

 This journal is © The Royal Society of Chemistry 2023

Open Access Article. Published on 06 2023. Downloaded on 01.02.26 6:57:40.
This article is licensed under a Creative Commons Attribution 3.0 Unported Licence.

At the dawn of this new era, we find challenges to the established understanding of the interstellar organic inventory. Indeed, McGuire *et al.* themselves could not explain the observed abundance of CNN through their state-of-the-art astrochemical modeling.[1] Their model, which performs well for smaller nitriles,[5] underestimates the observed abundance of CNN by six orders of magnitude.[1]

In a recent report,[6] we addressed this gap by elucidating the main destruction pathway for one of the two CNN isomers, which are expected to behave similarly and indeed have comparable abundances in TMC-1.[1] We found, contrary to the explicit assumption of McGuire *et al.*, that 1-cyanonaphthalene (1-CNN) is efficiently stabilized by rapid radiative cooling following ionization, closing off some of the reaction channels assumed to deplete CNN from TMC-1. Specifically, the model of McGuire *et al.* includes several charge transfer reactions:

$$A^+ + C_{10}H_7CN \rightarrow A + C_{10}H_7CN^+ \quad (1)$$

where A = C, H, or He, and where the resulting $C_{10}H_7CN^+$ is assumed to disintegrate into linear fragments. We show that the excess energies of these reactions (the difference between the ionization energies of the reactants) is insufficient to induce such thorough fragmentation and will mainly activate the lowest-energy unimolecular dissociation channel:

$$C_{10}H_7CN^+ \rightarrow C_{10}H_6^+ + HCN + \varepsilon, \quad (2)$$

where ε is the kinetic energy released in the reaction. Owing to efficient radiative stabilization by Recurrent Fluorescence (RF), the emission of optical photons from thermally populated electronically excited states,[7,8] even this low-energy channel is closed for collision with C^+ and at least partially closed for H^+.[6]

Crucially, vibronic coupling greatly increases the RF rate. RF, which is common for small PAHs,[9–16] has important implications for astrochemistry beyond the case of CNN in TMC-1. Stabilized by RF, small PAHs may be much more abundant in space than hitherto thought, including in more diffuse regions where it has long been held that PAHs must include at least ≈ 50 carbon atoms to survive in the UV radiation field there.[17] Better understanding of the RF mechanism and its competition with destructive reaction pathways can serve to refine candidate lists for astronomical searches for interstellar PAHs.

Recurrent Fluorescence of PAHs excited by UV photons has been suggested as the source of the Extended Red Emission (ERE)[18,19] observed in the red rectangle and other reflection nebulae. The ERE is a broad feature whose peak wavelength shifts in different astronomical environments.[18] Improved models of RF in PAHs, including vibronic couplings and anharmonic effects, and predicting excitation energy dependent emission spectra, are needed for quantitative comparison to astronomical observations.

In the present contribution, we extend our previous study by measuring the laser-induced dissociation rate and Kinetic Energy Release (KER) distributions of 1-CNN cations isolated in a cryogenic electrostatic ion-beam storage ring. This novel combination of techniques allows us to track the evolution of the internal energy distribution of the ions over four orders of magnitude in time after ionization. The measured cooling rate allows us to experimentally confirm our

Open Access Article. Published on 06 2023. Downloaded on 01.02.26 6:57:40.
This article is licensed under a Creative Commons Attribution 3.0 Unported Licence.

previously calculated Recurrent Fluorescence rate coefficient. Such laboratory studies are essential to understanding observations in the era of high-resolution astrochemistry.

2 Experiments

All experiments were conducted at the Double ElectroStatic Ion Ring ExpEriment (DESIREE) infrastructure at Stockholm University.[20,21] Cryogenic cooling of the storage ring, which is schematically shown in Fig. 1, to a temperature of approximately 13 K results in a residual gas density on the order of $\sim 10^4$ cm^{-3}, consisting mostly of H_2.[21] These conditions enable isolation of highly excited ions or reactive ions in a collision free environment for hours.[22,23] Electrostatic ion storage devices feature sampling times exceeding 1 s, orders of magnitude longer than conventional mass spectrometers, enabling time-resolved observations of delayed processes such as unimolecular dissociation[16] and thermionic electron emission.[24] DESIREE has also been used for vibrational energy dependent action spectroscopy of astrophysically relevant ions including PAHs,[25,26] substituted PAHs thought to form in interstellar ices,[27,28] and carbon cluster anions.[29,30]

The methods used here have largely been described previously.[6,16] Briefly, 1-CNN (Sigma-Aldrich, >96%) was sublimed from powder in a resistively heated oven coupled to an electron cyclotron resonance (ECR) ion source (Pantechnik Monogan) using helium as a support gas. Cations extracted from the source were accelerated to 34 keV kinetic energy. Mass-selected beams of 1-CNN$^+$ ($m/z = 153$) were stored in the DESIREE ion storage ring illustrated in Fig. 1.

The ion production method is known to produce ensembles of ions with broad vibrational energy distributions similar to Boltzmann distributions with temperatures of a few thousand Kelvin.[16] A small fraction of ions are produced with vibrational energies within a window such that their dissociation rate coefficients are low enough that they reach the ring, but high enough so that they may dissociate before they are stabilized by radiative cooling. These ions contribute a rapidly decreasing yield of neutral fragments referred to as spontaneous decay in the first tens of milliseconds of ion storage. The majority of ions remain stored after the disappearance of this spontaneous signal.

Stored ions were overlapped collinearly with light from an Optical Parametric Oscillator (OPO) laser system in the interaction arm of the storage ring (upper straight section in Fig. 1). The OPO was operated at 250 Hz repetition rate and produced pulses of ~5 ns duration and ~5 μJ per pulse at 420 nm.

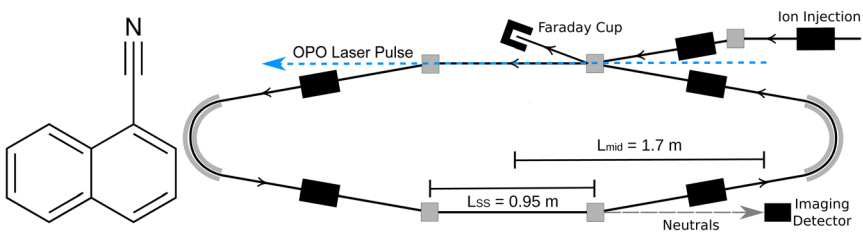

Fig. 1 (Left) Structure of 1-cyanonaphthalene ($C_{10}H_7CN$, 1-CNN). (Right) Schematic of DESIREE storage ring.

Open Access Article. Published on 06 2023. Downloaded on 01.02.26 6:57:40.
This article is licensed under a Creative Commons Attribution 3.0 Unported Licence.

Neutral fragments emitted in the observation arm of the storage ring (lower straight section in Fig. 1), which may occur up to several hundred microseconds after excitation, are unaffected by the electrostatic fields and continue on straight trajectories until they reach an imaging detector system with a triple stack of custom-made microchannel plates with ultra-high dynamic range (Photonis), a phosphor screen anode, and optical lenses projecting the phosphorescence through the DESIREE vacuum chamber windows and onto a CMOS camera (Photon Focus). The $\delta t = 2.0$ ms camera exposures were synchronized with the laser pulses, such that the laser-induced neutral yield resulting from each laser shot was collected in a single frame. Frames for a given laser firing time were summed over more than 50 000 repeat injections of 1-CNN^+, each of 400 ms storage duration.

For each summed frame, three-dimensional Newton spheres were reconstructed by applying an inverse Abel transform, using the 'three-point' algorithm implemented in the PyAbel package[31] written in Python. The density distribution is related to the KER distribution by:

$$\varepsilon(r_{3D}) = \frac{m_{neut}}{m_{cat}} E_{Acc} \left(\frac{r_{3D}}{L}\right)^2 \quad (3)$$

where $\varepsilon(r_{3D})$ is the KER associated with a radial slice of the Newton sphere of radius r_{3D}, m_{neut} and m_{cat} are the masses of the neutral and cationic reaction products, $E_{Acc} = 34$ keV is the beam energy, and L is the distance traveled by the products from the point of reaction to the detector. For clarity of presentation, the KER distributions in Fig. 7 are plotted against an ε scale calculated according to eqn (3) with $L = L_{mid}$, where $L_{mid} = 1.7$ m is the distance from the detector to the mid-point of the observation arm. Our analysis accounts for dissociation occurring along the full length of the observation arm by summing contributions to the Newton sphere density distribution in the detector plane from points at distances in the range $L_{mid} \pm L_{SS}/2$, where $L_{SS} = 0.95$ m is the length of the straight section seen by the detector (see Fig. 1). In the present case, the procedure gives a nearly insignificant correction relative to assuming all decays occur at L_{mid}.

3 Results

3.1 Dissociation rates

The spontaneous dissociation rate of the source-heated ions $R(t)$ is shown in the upper panel of Fig. 2. A constant background rate due to detector dark noise and collisions with residual gas has been subtracted. Due to the broad distribution $g(E, t)$ of vibrational energies E and the rapid variation of the dissociation rate coefficient $k_{diss}(E)$ with energy, the dissociation rate $R(t) \propto \int k_{diss}(E) g(E, t) dE$ does not follow simple exponential decay[32] but rather has the approximate time dependence[33]

$$R(t) = r_0 t^{-1} e^{-k_c t} \quad (4)$$

where t is the time after ion formation and $k_c = 302.9(4)$ s^{-1} is the critical rate coefficient at which dissociation and radiative cooling are competitive. The dashed line in the upper panel of Fig. 2 is a fit of eqn (4) to the data. Note that at longer times significant deviation from the exponential quenching behaviour is

Open Access Article. Published on 06 2023. Downloaded on 01.02.26 6:57:40.
This article is licensed under a Creative Commons Attribution 3.0 Unported Licence.

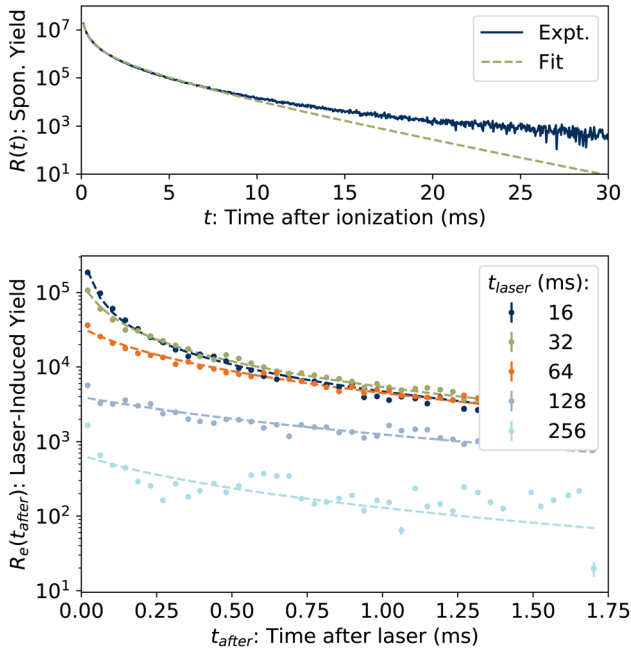

Fig. 2 (Top) Spontaneous dissociation rate $R(t)$, fit of eqn (4). (Bottom) Examples of laser-induced dissociation rates $R_e(t_{after})$ with fits of eqn (8).

observed. This effect is discussed in Section 4. The constant r_0 in eqn (4) contains the instrumental parameters and is given by:

$$r_0 = \eta_{det} N(t) \gamma_0(t) \frac{L_{SS}}{C} \quad (5)$$

where $\eta_{det} = 0.34(3)$ is the efficiency for detection of HCN (eqn (2)), $C = 8.7$ m is the circumference of the storage ring, $L_{SS} = 0.95$ m is the length of the stored beam viewed by the detector, and $N(t)$ is the average number of stored ions remaining in the ring at time t. The latter is determined from the count rate $R(t)$, measured during ion storage, and the terminal ion beam current, measured at the end of each injection–storage cycle using the Faraday cup shown in Fig. 1. The number $N(t)$ of ions stored during in the spontaneous decay measurement, relative to the initial number $N(120\ \mu s)$, is plotted in Fig. 3. The factor $\gamma_0(t)$ is the ensemble average destruction probability:[34]

$$\gamma_0(t) = \int g(E, t)(1 - e^{-k_{diss}(E)t}) dE / \int g(E, t) dE. \quad (6)$$

Put another way, it is the fraction of stored ions with vibrational energies $E \approx E_m$ consistent with lifetimes equal to the observation time, *i.e.* $k_{diss}(E_m) = t^{-1}$.[32] Simulated vibrational energy distributions $g(E, t)$ and $g_m(E, t) = g(E, t)(1 - e^{-k_{diss}(E)t})$ are plotted in the upper panel of Fig. 4 for a time $t = 120\ \mu s$ corresponding to the first pass of the ions through the storage ring. Also indicated are the vibrational energies E_{avg} and E_m averaged over the distributions $g(E, t)$ and $g_m(E, t)$, respectively.

Open Access Article. Published on 06 2023. Downloaded on 01.02.26 6:57:40.
This article is licensed under a Creative Commons Attribution 3.0 Unported Licence.

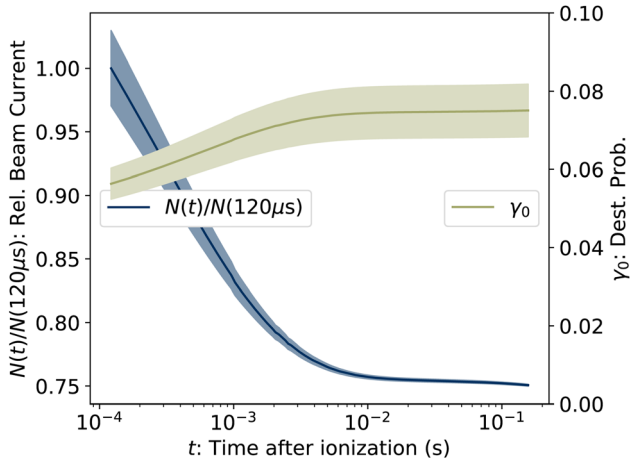

Fig. 3 (Left axis) Number of ions stored in the measurement of $R(t)$, relative to the value at the first time point at $t = 120$ μs. (Right axis) Ensemble averaged destruction probability γ_0, determined from eqn (5). The shaded areas give the uncertainties.

In the lower panel of Fig. 2, several examples of laser-induced decay rates R_e following single-photon absorption are plotted as functions of $t_{after} = t - t_{laser}$, the time after the laser was fired. At early laser firing times t_{laser} the laser-induced rate $R_e(t_{after})$ resembles the spontaneous decay rate $R(t)$, while at later times it converges on an exponential decay rate. We assume[35] that the portion of the ions which absorb a single photon of energy $h\nu$ is re-heated such that its internal energy distribution resembles that the full ensemble had at some earlier time $t_{laser} - \Delta t$, *i.e.*

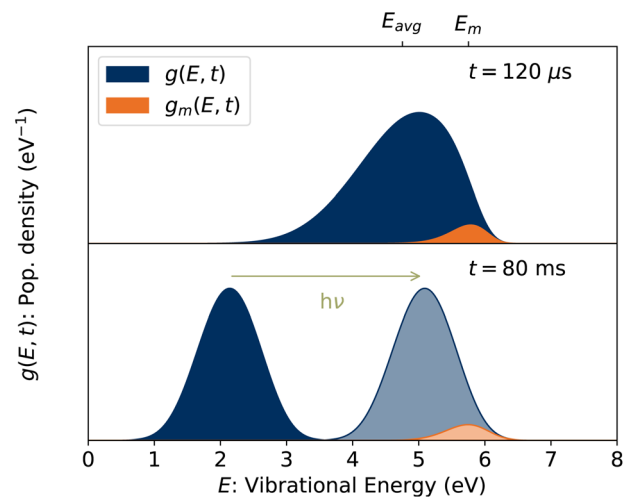

Fig. 4 (Top) Vibrational energy distribution of the stored ion ensemble, $g(E, t)$, and of the portion of the ensemble with energies $E \approx E_m$, $g_m(E, t)$, at $t = 120$ μs corresponding to the first pass of the ions through the ring. (Bottom) Vibrational energy distribution at a later time. Following the absorption of a single 420 nm photon, the ions in this example are reheated to the lighter shaded distribution and have the same value of E_m as in the upper panel.

$$g(E + h\nu,\ t_{\mathrm{laser}}) \propto g(E,\ t_{\mathrm{laser}} - \Delta t) \tag{7}$$

and that the laser-induced decay rate is given by

$$R_{\mathrm{e}}\left(t_{\mathrm{after}}\right) = \frac{p_1 L_{\mathrm{SS}}}{C} R(t + t_0) = \frac{p_1 L_{\mathrm{SS}} r_0}{C}(t + t_0)^{-1} \mathrm{e}^{-k_{\mathrm{c}}(t+t_0)} \tag{8}$$

where $t_0 = t_{\mathrm{laser}} - \Delta t$ is the time after formation to which the distribution is back-shifted, and p_1 is the probability of absorbing a single photon. The factor L_{SS}/C enters eqn (8) as the laser and ion beams are only overlapped in the outer straight section of the storage ring (see Fig. 1). The solid lines in the lower panel of Fig. 2 are fits to eqn (8) with the parameter k_{c} fixed to the value extracted from the fit of eqn (4) to the spontaneous decay rate. However, as eqn (4) gives a poor fit to $R(t)$ at later times, the values of t_0 were determined instead by fitting $R_{\mathrm{e}}(t_{\mathrm{after}})$ directly to $R(t)$, as illustrated in Fig. 5. A simultaneous fit to 100 laser-induced decay curves using a single constant value of $p_1 = 3.04(3) \times 10^{-3}$ in eqn (8) yielded the results shown in Fig. 6.

3.2 Kinetic energy release distributions

Examples of the kinetic energy release distributions $P_{\mathrm{e}}(\varepsilon)$ resulting from dissociation of laser-excited 1-CNN$^+$ are shown in Fig. 7. In our previous study of spontaneous dissociation of source-heated 1-CNN$^+$, we found that the KER distributions were well represented by the transition state model of Hansen,[36] which includes both tunneling through and reflection from a parabolic barrier:

$$P(\varepsilon) \propto \frac{\mathrm{e}^{\beta'}}{\mathrm{e}^{\beta'} + 1}\ \mathrm{e}^{-(\varepsilon - \Delta E)/k_{\mathrm{B}} T^{\ddagger}},$$
$$\text{where}\ \ \beta' = 4\pi \frac{\Delta E}{\hbar\omega}\left(\sqrt{\frac{\varepsilon}{\Delta E}} - 1\right). \tag{9}$$

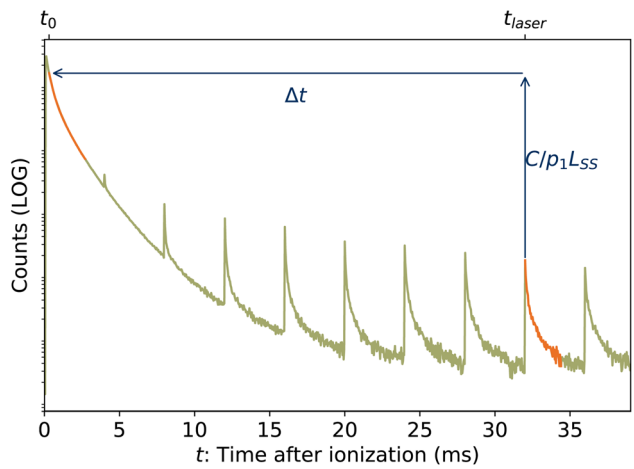

Fig. 5 Graphical example of method for determining back-shifted times t_0 by fitting the laser-induced dissociation rate $R_{\mathrm{e}}(t_{\mathrm{after}})$ to the spontaneous dissociation rate of source-heated ions $R(t)$. In this example, $t_{\mathrm{laser}} = 32$ ms and $t_0 = 320$ μs.

 This journal is © The Royal Society of Chemistry 2023

Open Access Article. Published on 06 2023. Downloaded on 01.02.26 6:57:40.
This article is licensed under a Creative Commons Attribution 3.0 Unported Licence.

Open Access Article. Published on 06 2023. Downloaded on 01.02.26 6:57:40.
This article is licensed under a Creative Commons Attribution 3.0 Unported Licence.

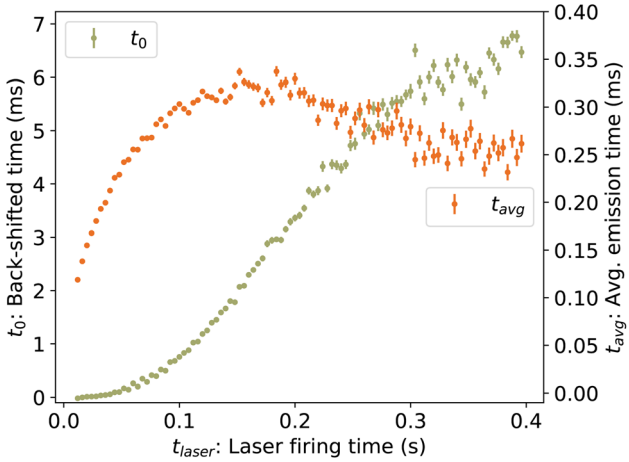

Fig. 6 (Left axis) Back-shifted times t_0 to which the vibrational energy distribution is re-heated following photon absorption at time t_{laser}, determined from laser-induced decay curves $R_e(t_{after})$. (Right axis) Average emission times t_{avg}.

We adopt the parameters from our earlier study,[6] which found a rather small reverse barrier height $\Delta E = 7.6(4)$ meV and a transition state frequency $\hbar\omega = 350(20)$ cm^{-1} from simultaneous fits to the KER distributions for spontaneously decaying 1-CNN$^+$ up to 20 ms after ionization. That study also found the dissociation rate coefficient to follow a modified Arrhenius expression:

$$k_{diss}(T^{\ddagger}) = \frac{k_B T^{\ddagger}}{h} e^{-E_a/k_B T^{\ddagger}} \quad (10)$$

with an activation energy for HCN-loss of $E_a = 3.16(4)$ eV. In the present contribution, all 100 laser-induced KER distributions are simultaneously fit subject to

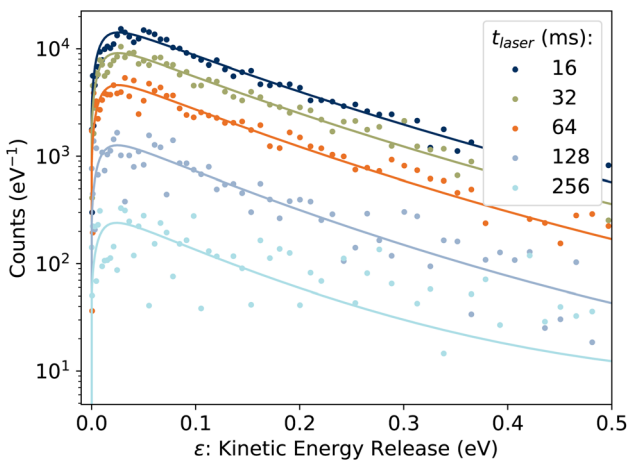

Fig. 7 Examples of KER distributions $P_e(\varepsilon)$ resulting from dissociation of laser-excited 1-CNN$^+$. Solid lines are fits to eqn (9).

Open Access Article. Published on 06 2023. Downloaded on 01.02.26 6:57:40.
This article is licensed under a Creative Commons Attribution 3.0 Unported Licence.

the physical constraint that the integrated distribution be equal to the integral of the count rate:

$$\int P_e(\varepsilon, t)\mathrm{d}\varepsilon = \int R_e(t)\mathrm{d}t = \frac{p_1 L_{SS} r_0}{C} k_{diss}\left(T^{\ddagger}\right)\delta t \tag{11}$$

where $\delta t = 2$ ms is the integration time of the camera and the value of $p_1 = 3.04(3) \times 10^{-3}$ determined from the fit of the laser-induced decay rates was held fixed. The values of $T^{\ddagger}$ resulting from the fit are plotted in Fig. 8.

To convert the transition state temperatures $T^{\ddagger}$ to the typical energies E_m of dissociation ions, the caloric curve $E(T)$ is first computed assuming Boltzmann statistics:

$$E(T) = \frac{\int E'\rho(E')\mathrm{e}^{-E'/k_B T}\,\mathrm{d}E'}{\int \rho(E')\mathrm{e}^{-E'/k_B T}\,\mathrm{d}E'} \tag{12}$$

where $\rho(E)$ is the vibrational level density calculated using the Beyer–Swinehart algorithm[37] and vibrational frequencies calculated at the B3LYP/6-31G(d,p) level of Density Functional Theory (DFT) as implemented in Gaussian 16.[38] Finally, the energy E_m of the precursor ion includes a finite heat bath correction due to the energy required to reach the transition state:[39]

$$E_m = E(T^{\ddagger}) + \frac{E_a}{2} + \frac{{E_a}^2}{12(E(T^{\ddagger}) + E_a/2)}. \tag{13}$$

In this energy range, the values of E_m depend linearly on $T^{\ddagger}$, as indicated by the second vertical axis in Fig. 8.

In Fig. 9, the experimentally-determined dissociation rate coefficient k_{diss} extracted using eqn (11) is plotted against the vibrational energy E_m from eqn (13), labeled E to emphasize that this is an intrinsic property not dependent on the

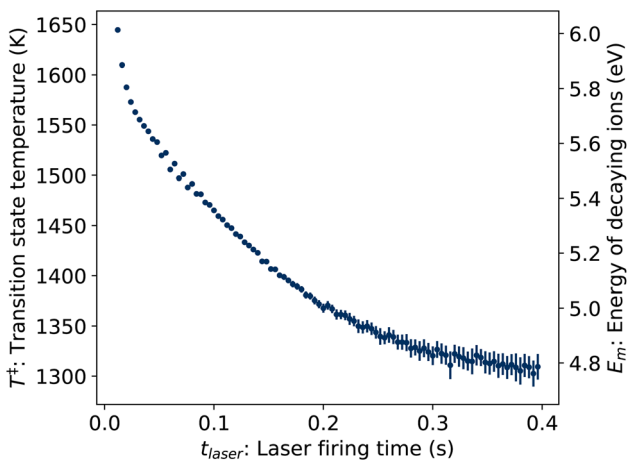

Fig. 8 Transition state temperatures $T^{\ddagger}$ (left axis) and corresponding vibrational energies E_m (right axis) of ions decaying following photon absorption at time t_{laser}, determined from KER distributions $P_e(\varepsilon)$.

Open Access Article. Published on 06 2023. Downloaded on 01.02.26 6:57:40.
This article is licensed under a Creative Commons Attribution 3.0 Unported Licence.

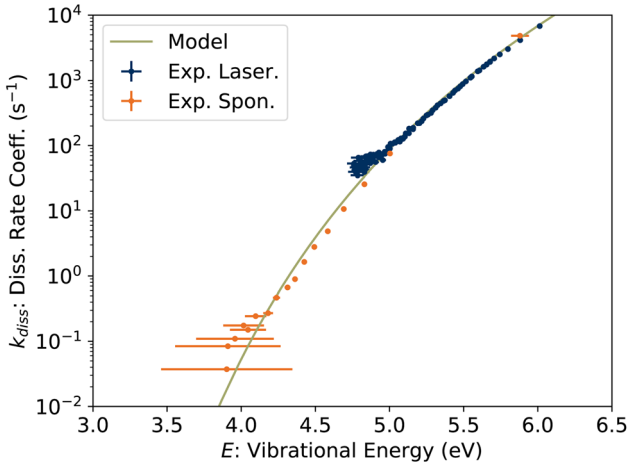

Fig. 9 Unimolecular dissociation rate coefficient $k_{diss}(E)$ from KER measurements.

internal energy distribution. The values from our previous study of spontaneous dissociation of 1-CNN$^+$ are also reproduced, along with our model dissociation rate coefficient in microcanonical form:

$$k_{diss}(E) = A^{diss}_{1000K} \frac{\rho(E - E_a)}{\rho(E)}, \quad (14)$$

where a nominal value of the pre-exponential factor $A^{diss}_{1000K} = k_B[1000K]/h = 2 \times 10^{13}$ s^{-1} was adopted.[6]

3.3 Cooling rate

To determine the cooling rate, we combine the back-shifted times t_0 from the decay rates with the corresponding energies E_m from the KER distributions. As the images for the KER measurement are integrated over the full decay curve following each laser shot, over which time the energy is changing rapidly, we compute an average emission time $t_{avg} = \int tR_e(t)dt / \int R_e(t)dt$, plotted in Fig. 6. The time associated with each value of E_m is thus $t_0 + t_{avg}$. These values, labeled $E_m(t_0)$ for simplicity, are plotted in Fig. 10.

Also plotted in Fig. 10 are values from our previous study of spontaneously dissociating 1-CNN$^+$. The values $E_m(t)$ from 2.5–50 ms were recorded during the measurement of the spontaneous decay rate $R(t)$ reproduced in Fig. 2. The same correction for the average emission time during the camera exposure time has been applied. The point at 120 μs is from a separate single-pass measurement.

Finally, the energies of the ions at the times the laser is fired, $E_m(t_{laser})$, are plotted in Fig. 10. Naively, one might assume $E_m(t_{laser}) = E_m(t_0) - h\nu$. However, as illustrated in Fig. 4, the vibrational energy distribution of the laser-reheated ions is significantly narrower than the original distribution of the hot ions as they cool. The high-energy tail of the reheated distribution, $g_m(E + h\nu, t_{laser})$, is thus shifted up by less than if the full original distribution $g(E, t_0)$ had simply shifted down by $h\nu$. We note that the re-heated distribution $g(E + h\nu, t_{laser})$, unlike the original

Open Access Article. Published on 06 2023. Downloaded on 01.02.26 6:57:40.
This article is licensed under a Creative Commons Attribution 3.0 Unported Licence.

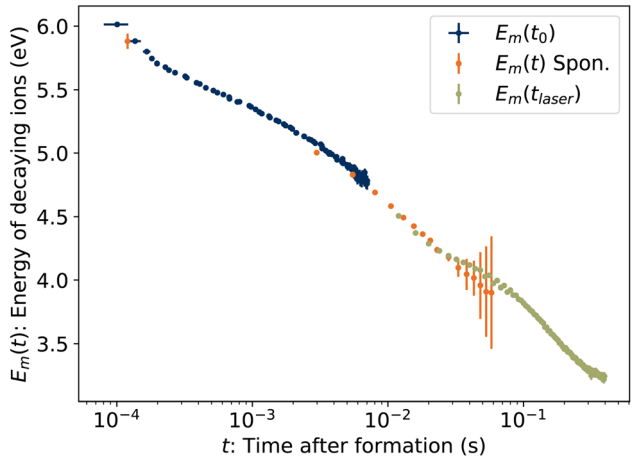

Fig. 10 Energies E_m of ions decaying at time t. Blue symbols $E_m t_0$ are the energies from Fig. 8 plotted against the back-shifted time $t_0 + t_{avg}$. The green symbols $E_m(t_{laser})$ give the energy in eqn (15) as a function of laser firing time. The orange symbols $E_m(t)$ are the energies of spontaneously decaying 1-CNN$^+$ determined previously.[6]

distribution $g(E, t_0)$, is approximately Gaussian and for such a distribution $E_m = E_{avg} + E_a$. Thus,

$$E_m(t_{laser}) = E(T^{\ddagger}) + E_a - h\nu. \quad (15)$$

These values are plotted in Fig. 10.

The time derivative of $E_m(t)$ is the rate at which the high-energy tail of the vibrational energy distribution $g_m(E, t)$ moves towards lower energy, be it by depletion of hot ions by dissociation or transposition of population by radiative cooling, and is called the energy shift rate. At any given time, only a small fraction γ_0 of the stored ion ensemble is part of the tail and subject to shift. Thus the total energy loss rate, which is directly comparable to the absolute dissociation and radiative cooling rate coefficients, is given by $\gamma_0^{-1}\, dE_m/dt$ and is plotted in Fig. 11. For clarity, points derived from laser firing times $t_{laser} > 300$ ms, which have large uncertainties due to the small changes in t_0 (see Fig. 6), are excluded from the plot but are included in the further analysis below.

Included in Fig. 11 are the calculated radiated powers P_{IR} and P_{RF} based on our previous study. Briefly, the IR (vibrational) radiative cooling rate coefficient is computed under the Simple Harmonic Cascade approximation:

$$k_{IR}(E) = \sum_s k_s = \sum_s A_s^{IR} \sum_{v=1}^{v \le E/h\nu_s} \frac{\rho(E - vh\nu_s)}{\rho(E)}, \quad (16)$$

where v is the vibrational quantum number, and $h\nu_s$ and A_s are the transition energy and Einstein coefficient of vibrational mode s, respectively, calculated at the B3LYP/6-31G(d,p) level of Density Functional Theory (DFT) as implemented in Gaussian 16.[38] The radiated power $P_{IR} = \sum_s k_s h\nu_s$. The RF (electronic) cooling rate coefficient is

Open Access Article. Published on 06 2023. Downloaded on 01.02.26 6:57:40.
This article is licensed under a Creative Commons Attribution 3.0 Unported Licence.

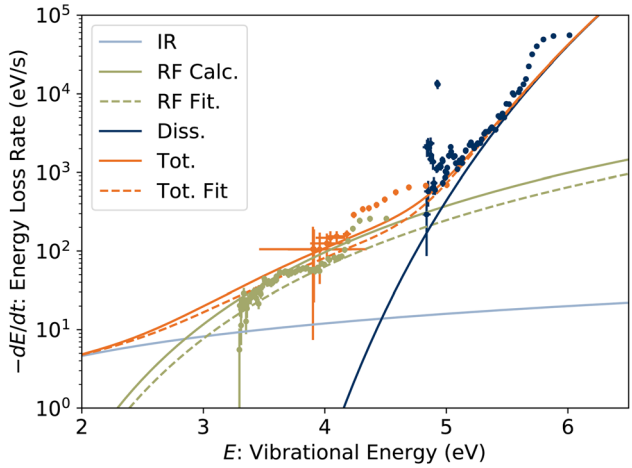

Fig. 11 Energy loss rate for 1-CNN$^+$. Symbol colours for experimental data correspond to those in Fig. 10. Solid lines are calculated energy loss rates due to dissociation, RF and IR radiative cooling. The dashed lines are a fit to the experimental data taking the oscillator strength f of the RF transition as a free parameter.

$$k_{\mathrm{RF}}(E) = A^{\mathrm{RF}} \frac{\rho(E - h\nu_{\mathrm{el}})}{\rho(E)}, \tag{17}$$

where the electronic transition energy $h\nu_{\mathrm{el}} = 1.10$ eV was computed at the equilibrium geometry of the lowest-lying L_α excited state using EOM-CCSD/cc-pVDZ calculations performed in CFOUR.[40] The Einstein coefficient is given by

$$A^{\mathrm{RF}} = \frac{2\pi {\nu_{\mathrm{el}}}^2 e^2}{\varepsilon_0 m_{\mathrm{e}} c^3} f, \tag{18}$$

where the oscillator strength $f = 0.011$ was calculated using a Franck–Condon–Herzberg–Teller simulation[41] at the ωB97X-D/cc-pVDZ level of DFT. The radiated power is $P_{\mathrm{RF}} = k_{\mathrm{RF}} h\nu_{\mathrm{el}}$. The energy shift rate due to dissociation is $P_{\mathrm{diss}} = k_{\mathrm{diss}} E$ where the dissociation rate coefficient is given in eqn (14).

The calculated energy loss rates agree well with the experimental values. In the range from 3 to 5 eV, the experimental points are up to two orders of magnitude greater than can be attributed to IR radiative cooling, and agrees well with our modeled P_{RF}. In our previous report, we found that Herzberg–Teller vibronic coupling increases the oscillator strength of the RF transition from 1×10^{-4} to the value $f = 0.011$ used in the calculated P_{RF}. If the oscillator strength is taken as a fitting parameter, holding the RF transition energy $h\nu_{\mathrm{el}}$, P_{IR} and P_{diss} constant, we find $f = 0.0074(3)$ to agree best with the experimental data, close to our calculated value. Energy loss rates with this lower oscillator strength are plotted with dashed lines in Fig. 11. Both modeled and fitted curves underpredict the measured loss rate in the range above 4 eV. Excluding the points derived from $E_{\mathrm{m}}(t_{\mathrm{laser}})$ (green symbols) covering the lower energy range from the fit (not shown) gives a somewhat higher $f = 0.0161(12)$. This range of values may suggest a dependence of the vibronic coupling strength, and hence f, the on vibrational energy, which could explain the non-exponential quenching of $R(t)$ (Fig. 2).

Open Access Article. Published on 06 2023. Downloaded on 01.02.26 6:57:40.
This article is licensed under a Creative Commons Attribution 3.0 Unported Licence.

4 Conclusions

By direct measurement of the energy loss rates of 1-CNN cations isolated in a cryogenic electrostatic ion-beam storage ring, we have confirmed that 1-CNN$^+$ is rapidly stabilized by recurrent fluorescence in the crucial energy range from 3–5 eV. Given the 8.6 eV ionization energy of 1-CNN, RF closes off some of the collisional destruction channels included in the model of McGuire *et al.*,[1] and completely forestalls photodissociation at photon energies found in molecular clouds.[42]

The non-exponential quenching of the spontaneous dissociation rate $R(t)$ (Fig. 2) has been observed previously for other PAHs, and has been attributed to sequential fragmentation of ionic products close enough in mass to the precursor to remain stored in the ring.[27] An alternative hypothesis is that the simple statistical model of RF (eqn (17)), which was first proposed by Boissel *et al.*,[8] does not fully capture the photophysics of RF in PAHs. Energy dependent oscillator strengths and/or emission wavelengths could lead to competition between dissociation and RF over a broader range of energies and thus non-exponential quenching. In the present results, the measured power radiated through RF is in good agreement with the simple model of Boissel *et al.*, with an oscillator strength lowest optical transition in 1-CNN$^+$ of $f = 0.0074(3)$. This is consistent with our previously calculated value of $f = 0.011$, nearly two orders of magnitude greater than if Herzberg–Teller vibronic coupling is neglected.[6] Improvements to the RF model, including energy-dependent f-values and emission wavelengths, can be expected to improve agreement with laboratory data. Consideration of Herzberg–Teller coupling is essential to modeling the radiative stabilization of isolated PAHs, as well as their optical spectra.

While the radiated power is the key quantity for predicting stability of isolated PAHs in astronomical environments, it does not completely constrain the emission mechanism. For example, more frequent emission of somewhat lower-energy photons would give the same power. Additional experiments of the present type on other PAHs, as well as, crucially, direct-detection measurements of dispersed RF spectra, will enable more quantitative comparison to astronomical observations and models of *e.g.* the Extended Red Emission.

Author contributions

JENN: investigation, formal analysis, software, writing – review and editing. JNB: conceptualization, data curation, formal analysis, funding acquisition, investigation, project administration, writing – review and editing. HC: funding acquisition, resources, writing – review and editing. SI: investigation, writing – review and editing. MCJ: investigation, writing – review and editing. HTS: funding acquisition, resources, supervision, writing – review and editing. HZ: funding acquisition, resources, supervision, writing – review and editing. BZ: investigation, writing – review and editing. MHS: conceptualization, data curation, formal analysis, funding acquisition, investigation, methodology, project administration, software, supervision, visualization, writing – original draft.

Conflicts of interest

There are no conflicts to declare.

Open Access Article. Published on 06 2023. Downloaded on 01.02.26 6:57:40.
This article is licensed under a Creative Commons Attribution 3.0 Unported Licence.

Acknowledgements

This work was supported by Swedish Research Council grant numbers 2016-03675 (MHS), 2018-04092 (HTS), 2019-04379 (HC), 2020-03437 (HZ), Knut and Alice Wallenberg Foundation grant number 2018.0028 (HC, HTS, and HZ), Olle Engkvist Foundation grant number 200-575 (MHS), and Swedish Foundation for International Collaboration in Research and Higher Education (STINT) grant number PT2017-7328 (JNB and MHS). We acknowledge the DESIREE infrastructure for provisioning of facilities and experimental support, and thank the operators and technical staff for their invaluable assistance. The DESIREE infrastructure receives funding from the Swedish Research Council under the grant numbers 2017-00621 and 2021-00155. This article is based upon work from COST Action CA18212 – Molecular Dynamics in the GAS phase (MD-GAS), supported by COST (European Cooperation in Science and Technology).

Notes and references

1 B. A. McGuire, R. A. Loomis, A. M. Burkhardt, K. L. K. Lee, C. N. Shingledecker, S. B. Charnley, I. R. Cooke, M. A. Cordiner, E. Herbst, S. Kalenskii, M. A. Siebert, E. R. Willis, C. Xue, A. J. Remijan and M. C. McCarthy, *Science*, 2021, **371**, 1265–1269.

2 J. Cernicharo, M. Agúndez, C. Cabezas, B. Tercero, N. Marcelino, J. R. Pardo and P. de Vicente, *Astron. Astrophys.*, 2021, **649**, L15.

3 T. S.-Y. Lai, L. Armus, V. U, T. Díaz-Santos, K. L. Larson, A. Evans, M. A. Malkan, P. Appleton, J. Rich, F. Müller-Sánchez, H. Inami, T. Bohn, J. McKinney, L. Finnerty, D. R. Law, S. T. Linden, A. M. Medling, G. C. Privon, Y. Song, S. Stierwalt, P. P. van der Werf, L. Barcos-Muñoz, J. D. T. Smith, A. Togi, S. Aalto, T. Böker, V. Charmandaris, J. Howell, K. Iwasawa, F. Kemper, J. M. Mazzarella, E. J. Murphy, M. J. I. Brown, C. C. Hayward, J. Marshall, D. Sanders and J. Surace, *Astrophys. J., Lett.*, 2022, **941**, L36.

4 V. U, T. Lai, M. Bianchin, R. P. Remigio, L. Armus, K. L. Larson, T. Díaz-Santos, A. Evans, S. Stierwalt, D. R. Law, M. A. Malkan, S. Linden, Y. Song, P. P. van der Werf, T. Gao, G. C. Privon, A. M. Medling, L. Barcos-Muñoz, C. C. Hayward, H. Inami, J. Rich, S. Aalto, P. Appleton, T. Bohn, T. Böker, M. J. I. Brown, V. Charmandaris, L. Finnerty, J. Howell, K. Iwasawa, F. Kemper, J. Marshall, J. M. Mazzarella, J. McKinney, F. Muller-Sanchez, E. J. Murphy, D. Sanders and J. Surace, *Astrophys. J., Lett.*, 2022, **940**, L5.

5 B. A. McGuire, A. M. Burkhardt, S. Kalenskii, C. N. Shingledecker, A. J. Remijan, E. Herbst and M. C. McCarthy, *Science*, 2018, **359**, 202–205.

6 M. H. Stockett, J. N. Bull, H. Cederquist, S. Indrajith, M. Ji, J. E. Navarro Navarrete, H. T. Schmidt, H. Zettergren and B. Zhu, *Nat. Commun.*, 2023, **14**, 395.

7 A. Léger, P. Boissel and L. d'Hendecourt, *Phys. Rev. Lett.*, 1988, **60**, 921–924.

8 P. Boissel, P. de Parseval, P. Marty and G. Lefèvre, *J. Chem. Phys.*, 1997, **106**, 4973–4984.

9 S. Martin, J. Bernard, R. Brédy, B. Concina, C. Joblin, M. Ji, C. Ortega and L. Chen, *Phys. Rev. Lett.*, 2013, **110**, 063003.

10 M. Ji, G. Montagne, R. Brédy, J. Bernard, L. Chen and S. Martin, *Phys. Scr.*, 2013, **T156**, 014092.

Open Access Article. Published on 06 2023. Downloaded on 01.02.26 6:57:40.
This article is licensed under a Creative Commons Attribution 3.0 Unported Licence.

11 S. Martin, M. Ji, J. Bernard, R. Brédy, B. Concina, A. R. Allouche, C. Joblin, C. Ortega, G. Montagne, A. Cassimi, Y. Ngono-Ravache and L. Chen, *Phys. Rev. A*, 2015, **92**, 053425.
12 R. Brédy, C. Ortéga, M. Ji, L. Chen, J. Bernard, A. R. Allouche, C. Joblin, A. Cassimi and S. Martin, *J. Phys.: Conf. Ser.*, 2015, **583**, 012042.
13 M. Ji, J. Bernard, L. Chen, R. Brédy, C. Ortéga, C. Joblin, A. Cassimi and S. Martin, *J. Chem. Phys.*, 2017, **146**, 044301.
14 J. Bernard, L. Chen, R. Brédy, M. Ji, C. Ortéga, J. Matsumoto and S. Martin, *Nucl. Instrum. Methods Phys. Res., Sect. B*, 2017, **408**, 21–26.
15 M. Saito, H. Kubota, K. Yamasa, K. Suzuki, T. Majima and H. Tsuchida, *Phys. Rev. A*, 2020, **102**, 012820.
16 M. H. Stockett, J. N. Bull, J. T. Buntine, E. Carrascosa, M. Ji, N. Kono, H. T. Schmidt and H. Zettergren, *J. Chem. Phys.*, 2020, **153**, 154303.
17 A. Li, *Nat. Astron.*, 2020, **4**, 339–351.
18 A. N. Witt and T. S.-Y. Lai, *Astrophys. Space Sci.*, 2020, **365**, 58.
19 T. S.-Y. Lai, A. N. Witt, C. Alvarez and J. Cami, *Mon. Not. R. Astron. Soc.*, 2020, **492**, 5853–5864.
20 R. D. Thomas, H. T. Schmidt, G. Andler, M. Björkhage, M. Blom, L. Brännholm, E. Bäckström, H. Danared, S. Das, N. Haag, P. Halldén, F. Hellberg, A. I. S. Holm, H. A. B. Johansson, A. Källberg, G. Källersjö, M. Larsson, S. Leontein, L. Liljeby, P. Löfgren, B. Malm, S. Mannervik, M. Masuda, D. Misra, A. Orbán, A. Paál, P. Reinhed, K.-G. Rensfelt, S. Rosén, K. Schmidt, F. Seitz, A. Simonsson, J. Weimer, H. Zettergren and H. Cederquist, *Rev. Sci. Instrum.*, 2011, **82**, 065112.
21 H. T. Schmidt, R. D. Thomas, M. Gatchell, S. Rosén, P. Reinhed, P. Löfgren, L. Brännholm, M. Blom, M. Björkhage, E. Bäckström, J. D. Alexander, S. Leontein, D. Hanstorp, H. Zettergren, L. Liljeby, A. Källberg, A. Simonsson, F. Hellberg, S. Mannervik, M. Larsson, W. D. Geppert, K. G. Rensfelt, H. Danared, A. Paál, M. Masuda, P. Halldén, G. Andler, M. H. Stockett, T. Chen, G. Källersjö, J. Weimer, K. Hansen, H. Hartman and H. Cederquist, *Rev. Sci. Instrum.*, 2013, **84**, 055115.
22 E. Bäckström, D. Hanstorp, O. M. Hole, M. Kaminska, R. F. Nascimento, M. Blom, M. Björkhage, A. Källberg, P. Löfgren, P. Reinhed, S. Rosén, A. Simonsson, R. D. Thomas, S. Mannervik, H. T. Schmidt and H. Cederquist, *Phys. Rev. Lett.*, 2015, **114**, 143003.
23 M. Gatchell, J. Ameixa, M. Ji, M. H. Stockett, A. Simonsson, S. Denifl, H. Cederquist, H. T. Schmidt and H. Zettergren, *Nat. Commun.*, 2021, **12**, 6646.
24 M. H. Stockett, J. N. Bull, J. T. Buntine, E. Carrascosa, E. K. Anderson, M. Gatchell, M. Kaminska, R. F. Nascimento, H. Cederquist, H. T. Schmidt and H. Zettergren, *Eur. Phys. J. D*, 2020, **74**, 150.
25 M. H. Stockett, M. Björkhage, H. Cederquist, H. Schmidt and H. Zettergren, *Faraday Discuss.*, 2019, **217**, 126–137.
26 M. H. Stockett, M. Björkhage, H. Cederquist, H. T. Schmidt and Z. Henning, *Proc. Int. Astron. Union*, 2019, **15**, 127–131.
27 M. H. Stockett, J. N. Bull, H. Schmidt and H. Zettergren, *Phys. Chem. Chem. Phys.*, 2022, **24**, 12002–12010.
28 B. Zhu, J. N. Bull, M. Ji, H. Zettergren and M. H. Stockett, *J. Chem. Phys.*, 2022, **157**, 044303.

Open Access Article. Published on 06 2023. Downloaded on 01.02.26 6:57:40.
This article is licensed under a Creative Commons Attribution 3.0 Unported Licence.

29 J. N. Bull, M. S. Scholz, E. Carrascosa, M. K. Kristiansson, G. Eklund, N. Punnakayathil, N. de Ruette, H. Zettergren, H. T. Schmidt, H. Cederquist and M. H. Stockett, *J. Chem. Phys.*, 2019, **151**, 114304.
30 B. Zhu, J. N. Bull, J. E. Navarro Navarrete, A. F. Schmidt-May, H. Cederquist, H. T. Schmidt, H. Zettergren and M. H. Stockett, *J. Chem. Phys.*, 2022, **157**, 174308.
31 S. Gibson, D. D. Hickstein, R. Yurchak, M. Ryazanov, D. Das and G. Shih, *PyAbel: v0.8.4*, 2021, DOI: **10.5281/zenodo.7438595**.
32 K. Hansen, J. U. Andersen, P. Hvelplund, S. P. Møller, U. V. Pedersen and V. V. Petrunin, *Phys. Rev. Lett.*, 2001, **87**, 123401.
33 J. Andersen, H. Cederquist, J. Forster, B. Huber, P. Hvelplund, J. Jensen, B. Liu, B. Manil, L. Maunoury, S. Brøndsted Nielsen, U. Pedersen, H. Schmidt, S. Tomita and H. Zettergren, *Eur. Phys. J. D*, 2003, **25**, 139–148.
34 K. Hansen, *Phys. Rev. A*, 2020, **102**, 052823.
35 A. E. K. Sundén, M. Goto, J. Matsumoto, H. Shiromaru, H. Tanuma, T. Azuma, J. U. Andersen, S. E. Canton and K. Hansen, *Phys. Rev. Lett.*, 2009, **103**, 143001.
36 K. Hansen, *Chem. Phys. Lett.*, 2018, **693**, 66–71.
37 T. Beyer and D. F. Swinehart, *Commun. ACM*, 1973, **16**, 379.
38 M. J. Frisch, G. W. Trucks, H. B. Schlegel, G. E. Scuseria, M. A. Robb, J. R. Cheeseman, G. Scalmani, V. Barone, B. Mennucci, G. A. Petersson, H. Nakatsuji, M. Caricato, X. Li, H. P. Hratchian, A. F. Izmaylov, J. Bloino, G. Zheng, J. L. Sonnenberg, M. Hada, M. Ehara, K. Toyota, R. Fukuda, J. Hasegawa, M. Ishida, T. Nakajima, Y. Honda, O. Kitao, H. Nakai, T. Vreven, J. A. Montgomery Jr, J. E. Peralta, F. Ogliaro, M. Bearpark, J. J. Heyd, E. Brothers, K. N. Kudin, V. N. Staroverov, R. Kobayashi, J. Normand, K. Raghavachari, A. Rendell, J. C. Burant, S. S. Iyengar, J. Tomasi, M. Cossi, N. Rega, J. M. Millam, M. Klene, J. E. Knox, J. B. Cross, V. Bakken, C. Adamo, J. Jaramillo, R. Gomperts, R. E. Stratmann, O. Yazyev, A. J. Austin, R. Cammi, C. Pomelli, J. W. Ochterski, R. L. Martin, K. Morokuma, V. G. Zakrzewski, G. A. Voth, P. Salvador, J. J. Dannenberg, S. Dapprich, A. D. Daniels, Ã. Farkas, J. B. Foresman, J. V. Ortiz, J. Cioslowski and D. J. Fox, *Gaussian 16 Revision B.01*, Gaussian Inc., Wallingford CT, 2016.
39 J. Andersen, E. Bonderup and K. Hansen, *J. Chem. Phys.*, 2001, **114**, 6518–6525.
40 J. F. Stanton, J. Gauss, L. Cheng, M. E. Harding, D. A. Matthews and P. G. Szalay, *CFOUR, Coupled-Cluster Techniques for Computational Chemistry, a Quantum-Chemical Program Package*.
41 F. Santoro, A. Lami, R. Improta, J. Bloino and V. Barone, *J. Chem. Phys.*, 2008, **128**, 224311.
42 K. I. Öberg, *Chem. Rev.*, 2016, **116**, 9631–9663.